

Interpreting Adversarial Examples by Activation Promotion and Suppression

Kaidi Xu¹, Sijia Liu², Gaoyuan Zhang², Mengshu Sun¹, Pu Zhao¹, Quanfu Fan², Chuang Gan², Xue Lin¹

¹ Northeastern University

² MIT-IBM Watson AI Lab, IBM Research

sijia.liu@ibm.com

Abstract

It is widely known that convolutional neural networks (CNNs) are vulnerable to adversarial examples: images with imperceptible perturbations crafted to fool classifiers. However, interpretability of these perturbations is less explored in the literature. This work aims to better understand the roles of adversarial perturbations and provide visual explanations from pixel, image and network perspectives. We show that adversaries have a promotion-suppression effect (PSE) on neurons' activations and can be primarily categorized into three types: i) suppression-dominated perturbations that mainly reduce the classification score of the true label, ii) promotion-dominated perturbations that focus on boosting the confidence of the target label, and iii) balanced perturbations that play a dual role in suppression and promotion. We also provide image-level interpretability of adversarial examples. This links PSE of pixel-level perturbations to class-specific discriminative image regions localized by class activation mapping (Zhou et al. 2016). Further, we examine the adversarial effect through network dissection (Bau et al. 2017), which offers concept-level interpretability of hidden units. We show that there exists a tight connection between the units' sensitivity to adversarial attacks and their interpretability on semantic concepts. Lastly, we provide some new insights from our interpretation to improve the adversarial robustness of networks.

1 Introduction

Adversarial examples are inputs crafted with the intention of fooling machine learning models (Carlini et al. 2016; Kurakin, Goodfellow, and Bengio 2016; Athalye, Carlini, and Wagner 2018; Xu et al. 2019a). Many existing works have shown that CNNs are vulnerable to adversarial examples with human imperceptible pixel-level perturbations. Different types of adversarial attacks were proposed with a high success rate of mis-classification. However, understanding these attacks and further interpreting their effects are so far less explored in the literature. In this work, we attempt to study some fundamental questions as follows: a) How to interpret the mechanism of adversarial perturbations at pixel and image levels? b) Rather than attack generation, how to explain the effectiveness of different adversarial attacks? c) How to explore the adversarial effects on the inter-

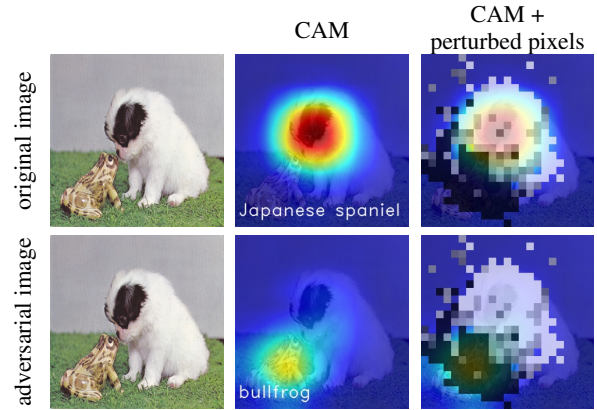


Figure 1: Explanation of adversarial perturbations produced by the C&W attack (Carlini and Wagner 2017b). The first column shows the original image (with true label ‘Japanese spaniel’) and its adversarial example (with target label ‘bullfrog’). The second column demonstrates CAM of the original image with respect to the true label and CAM of the adversarial example with respect to the target label. At the third column, the adversarial perturbations are overlaid on CAM, and their effects are categorized by our approach: suppression-dominated perturbations (white, at the face of spaniel), promotion-dominated perturbations (black, at the face of bullfrog), and balance-dominated perturbations (gray).

nal response of CNNs? And d) how does the interpretability of adversarial examples help robustness?

Contributions. First, we study the sensitivity and functionality of pixel-level perturbations on image classification. Unlike adversarial saliency maps (ASMs) (Papernot et al. 2016a), our proposed sensitivity measure takes into account the dependency among pixels that contribute simultaneously to the classification confidence. We uncover the *promotion-suppression effect (PSE)* of adversarial perturbations. We group the adversaries into three types: a) *suppression-dominated perturbations* that mainly reduce the classification score of the true label, b) *promotion-dominated perturbations* that focus on boosting the confidence of the target label, and c) *balance-dominated perturbations* that play a dual role in suppression and promotion.

Second, we associate PSE of pixel-level perturbations

with image-level interpretability based on class activation map (CAM) (Zhou et al. 2016). We show that the adversarial pattern can be interpreted using the class-specific discriminative image regions. Figure 1 presents an example of the C&W adversarial attack (Carlini and Wagner 2017b), where suppression- and promotion-dominated perturbations are matched to the discriminative regions of the natural image (with respect to the true label ‘Japanese spaniel’) and those of the adversarial example (with respect to the target label ‘bullfrog’), respectively. We also show that the CAM-based image-level interpretability provides a means to evaluate the efficacy of attack generation methods. Although some works (Selvaraju et al. 2017; Xiao et al. 2018; Xu et al. 2019b) attempted to connect adversarial examples with CAM, they mainly focused on the visualization of adversarial examples.

Third, we present the first attempt to analyze the effect of adversarial examples on the internal representations of CNNs using the network dissection technique (Bau et al. 2017). We show a tight connection between the sensitivity of hidden units of CNNs and their interpretability on semantic concepts, which are also aligned with PSE. Furthermore, we provide some insights on how to improve robustness by leveraging our interpretation of adversarial examples.

Related Works. The effectiveness of adversarial attacks (Goodfellow, Shlens, and Szegedy 2015; Kurakin, Goodfellow, and Bengio 2017; Carlini and Wagner 2017b; Chen et al. 2017; Xu et al. 2019b; Ye et al. 2019) are commonly measured from attack success rate as well as ℓ_p -norm distortion between natural and adversarial examples. Some works (Karmon, Zoran, and Goldberg 2018; Brown et al. 2017) generated adversarial attacks by adding unconstrained noise patches, which are different from norm-ball constrained attacks, leading to higher noise visibility. Rather than attack generation, the goal of this paper is to understand and explain the effect of imperceptible perturbations. Here we focus on norm-ball constrained adversarial attacks. Many defense methods have also been developed against adversarial attacks. Examples include defensive distillation (Papernot et al. 2016b), random mask (Luo et al. 2018), training with a Lipschitz regularized loss function (Finlay, Oberman, and Abbasi 2018), and robust adversarial training using min-max optimization (Madry et al. 2017; Sinha, Namkoong, and Duchi 2018).

Although the study on attack generation and defense has attracted an increasing amount of attention, interpretability of these examples is less explored in the literature. Some preliminary works (Papernot et al. 2016a; Yu, Dong, and Chen 2018) were made on evaluating the impact of pixel-level adversarial perturbations on changing the classification results. In (Papernot et al. 2016a), Jacobian-based ASM was introduced to greedily perturb pixels that significantly contribute to the likelihood of target classification. However, ASM implicitly ignores the coupling effect of pixel-level perturbations, and it becomes less effective when an image has multiple color channels given the fact that each color channel is treated independently. As an extension of (Papernot et al. 2016a), the work (Yu, Dong, and Chen 2018) proposed an adversarial saliency prediction (ASP) method,

which characterizes the divergence of the ASM distribution and the distribution of perturbations.

Both ASM (Papernot et al. 2016a) and ASP (Yu, Dong, and Chen 2018) have helped humans to understand how adversarial perturbations made to inputs will affect the outputs of neural networks, however, it remains difficult to visually explain the mechanism of the adversary given the fact that pixel-level perturbations are small and imperceptible to humans. The work (Selvaraju et al. 2017; Xiao et al. 2018) adopted CAM to visualize the change of attention regions of the natural and adversarial images, but the use of CAM is preliminary and its connection with interpretability of pixel-level perturbations is missing. The most relevant work to ours is (Xu et al. 2019b), which proposed an interpretability score via ASM and CAM. However, it focuses on generating structure-driven adversarial attacks by promoting group sparsity of perturbations. In contrast, we provide more thorough and insightful quantitative analysis. In particular, we associate the class-specific discriminative image regions with pixel-level perturbations. We also show that the CAM-based interpretability provides means to examine the effectiveness of perturbation patterns.

From the network perspective, the work (Dong et al. 2017) investigated the effect of an ensemble attack on neurons’ activations. In (Carter et al. 2019), Activation Atlas was proposed to show feature visualizations of basis neurons as well as common combinations of neurons. And it was applied to visualizing the effect of adversarial patches (rather than norm-ball constrained adversarial perturbations). Different from (Carter et al. 2019; Dong et al. 2017), we adopt the technique of network dissection (Bau et al. 2017; 2019) to peer into the effect of adversarial examples on the concept-level interpretability of hidden units.

2 Preliminaries: Attack, Dataset, and Model

Let $\mathbf{x}_0 \in \mathbb{R}^n$ denote the *natural* image, and δ be *adversarial perturbation* to be designed. Here, unless specified otherwise, the vector representation of an image is used. The *adversarial example* is then given by $\mathbf{x}' = \mathbf{x}_0 + \delta$. By setting the input of the CNNs as \mathbf{x}_0 and \mathbf{x}' , the classifier will predict the true label t_0 and the target label t ($\neq t_0$), respectively. To find the minimum adversarial perturbation δ for misclassification from t_0 to t , a so-called norm-ball constrained attack technique is commonly used; Examples considered in this paper include **IFGSM** (Goodfellow, Shlens, and Szegedy 2015), **C&W** (Carlini and Wagner 2017a), **EAD** (Chen et al. 2017), and **Str** attacks (Xu et al. 2019b). We refer readers to Appendix 1 for more details on attack generation.

Our work attempts to interpret adversarial examples from the pixel (Sec. 3), image (Sec. 4) and network (Sec. 5) perspective. At pixel and image levels, we generate adversarial examples from ImageNet under network models Resnet_v2_101 (He et al. 2016) and Inception_v3 (Szegedy et al. 2016). At the network level, we generate adversarial examples from the Broadly and Densely Labeled Dataset (Brodén) (Bau et al. 2017), which contains examples with pixel-level concept annotations related to multiple concept categories including color, material, texture, part, scene and

object. The considered network model is Resnet_152 (He et al. 2016).

3 Effects of Pixel-level Perturbations

We begin by quantifying how much impact a perturbation could make on prediction confidence. We use the change of logit scores with respect to (w.r.t.) both correct and target labels to measure such an effect. This is in the similar spirit of the C&W attack loss (Carlini and Wagner 2017a) but we focus on grid region-level perturbations as well as the leave-one-out interpretability criterion (Yang et al. 2019). We build a pixel-level sensitivity measure that can be further used for image-level sensitivity analysis. We aim to answer the questions: How to tag the role of pixel-level perturbations? And how is the perturbation sensitivity associated with the perturbation strength?

Recall that $\mathbf{x} = \mathbf{x}_0$ denotes the natural image, and $\mathbf{x} = \mathbf{x}'$ corresponds to the adversarial example. We divide an image \mathbf{x} into m grid regions with coordinate sets $\{\mathcal{G}_i\}_{i=1}^m$, where each \mathcal{G}_i contains a group of pixels, and $\cup_{i=1}^m \mathcal{G}_i = [n]$. Here $[n]$ denotes the overall set of pixels $\{1, 2, \dots, n\}$. We note that a proper size of a grid region facilitates visual explanation on semantic image sub-regions and save computation cost. So we set it as 13×13 for ImageNet empirically and also consistent with (Xu et al. 2019b). Let $\delta_{\mathcal{G}_i} \in \mathbb{R}^n$ be the perturbation at the grid region \mathcal{G}_i , where $[\delta_{\mathcal{G}_i}]_j = \delta_j$ if $j \in \mathcal{G}_i$, and 0 otherwise. Here $[\mathbf{a}]_i$ or a_i denotes the i th element of \mathbf{a} . We next propose a sensitivity measure of $\delta_{\mathcal{G}_i}$, which characterizes the impact of pixel-level perturbations on the prediction confidence (in terms of logit score).

Definition 1 (Sensitivity measure of perturbations): *The impact of perturbation $\delta_{\mathcal{G}_i}$ on prediction is measured from two aspects: i) the logit change $d_{0,i}$ w.r.t. the true label t_0 , and ii) the logit change $d_{t,i}$ w.r.t. the target label t . That is,*

$$d_{0,i} = \max\{Z(\mathbf{x}' - \delta_{\mathcal{G}_i})_{t_0} - Z(\mathbf{x}')_{t_0}, \xi\}, \quad (1)$$

$$d_{t,i} = \max\{Z(\mathbf{x}')_t - Z(\mathbf{x}' - \delta_{\mathcal{G}_i})_t, \xi\}, \quad (2)$$

$$s_i = d_{0,i} + d_{t,i} \quad (3)$$

for $i \in [m]$, where $Z(\mathbf{x})_j$ gives the logit score with respect to class j , and $\xi > 0$ is a small positive number.

The rationale behind Definition 1 is that the adversarial example \mathbf{x}' , when it is successfully generated, makes the network misclassified from t_0 to t . Thus, we assign each $\delta_{\mathcal{G}_i}$ i) the change in the confidence of the true label t_0 and ii) the change in the confidence of the target label t when $\delta_{\mathcal{G}_i}$ is removed from the adversarial example \mathbf{x}' . The sensitivity measure in Definition 1 enjoys the similar spirit of leave-one-out interpretability (Zeiler and Fergus 2014; Yang et al. 2019), but the latter focuses on the prediction sensitivity of a single class rather than both t_0 and t .

In Definition 1, a large $d_{0,i}$ implies a more significant role of a perturbation $\delta_{\mathcal{G}_i}$ on *suppressing* the classification result away from t_0 . By contrast, $d_{t,i}$ measures the effect of $\delta_{\mathcal{G}_i}$ on *promoting* the prediction confidence of the target label. The overall adversarial significance s_i is the combined effect of $d_{0,i}$ and $d_{t,i}$. Thus, pixels with small values of s_i play less significant roles in misleading classifiers. In (1)–(2), we use

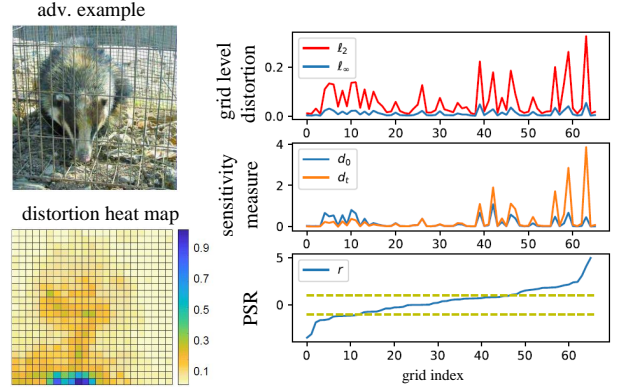


Figure 2: Illustration on sensitivity measure via the ‘badger’-to-‘computer’ adversarial example generated by C&W attack. Here the true label is ‘badger’ and the target label is ‘computer’. The first column shows the adversarial example and the heat map of ℓ_2 -norm distortion at each grid region, i.e., $\{\|\delta_{\mathcal{G}_i}\|_2\}$. The second column presents ℓ_p norm of $\delta_{\mathcal{G}_i}$ ($p = 2, \infty$), sensitivity scores $d_{0,i}$ and $d_{t,i}$, and PSR r_i versus the index of grid regions, where the dash lines correspond to the PSR threshold ± 1 .

ξ to get rid of the negative values of $d_{0,i}$ and $d_{t,i}$, i.e., the insignificant cases for the adversary.

With the aid of $\{d_{0,i}\}$ and $\{d_{t,i}\}$ in Definition 1, we define a promotion-suppression ratio (PSR)

$$r_i = \log_2(d_{t,i}/d_{0,i}), i \in [m], \quad (4)$$

which describes the mechanism of $\delta_{\mathcal{G}_i}$ on misclassification. In (4), the logarithm is taken for ease of studying PSR under different regimes, e.g. $r_i \geq 1$ implies that $d_{t,i} \geq 2d_{0,i}$. Here we categorize the effect of $\delta_{\mathcal{G}_i}$ into three types. If $r_i < -1$, then we call $\delta_{\mathcal{G}_i}$ a *suppression-dominated perturbation*, which is mainly used to reduce the classification logit of the true label. If $r_i > 1$, then we call $\delta_{\mathcal{G}_i}$ a *promotion-dominated perturbation*, which is mainly used to boost the classification logit of the target label. If $r_i \in [-1, 1]$, then we call $\delta_{\mathcal{G}_i}$ a *balance-dominated perturbation* that plays a dual role in suppression and promotion. Although different threshold values on r_i can be used, we choose ± 1 for ease of visual explanation. In Figure 2 we illustrate the sensitivity measures (1)–(4) through an adversarial example generated by the C&W attack (Carlini and Wagner 2017b). As we can see, either $d_{0,i}$ or $d_{t,i}$ (and thus s_i) is correlated with the perturbation strength at each grid region (in terms of the ℓ_p norm of $\delta_{\mathcal{G}_i}$). Also, PSR implies that most of perturbations in this example contribute to promoting the prediction confidence of the target class. This will also be verified by the image-level interpretability in Figure 4.

The example of the C&W attack in Figure 2 suggests that the strength of pixel-level perturbations (e.g., in terms of ℓ_2 norm) might be strongly correlated with the input sensitivity scores. For a more thorough quantitative analysis, we examine 5000 adversarial examples generated by 4 attack methods under 2 network models from ImageNet. In Figure 3, we present Pearson correlation and Kendall rank correlation between the distortion strength $\{\|\delta_{\mathcal{G}_i}\|_2\}$ and the proposed sensitivity scores $\{s_i\}$ given by (3). We see that C&W, EAD

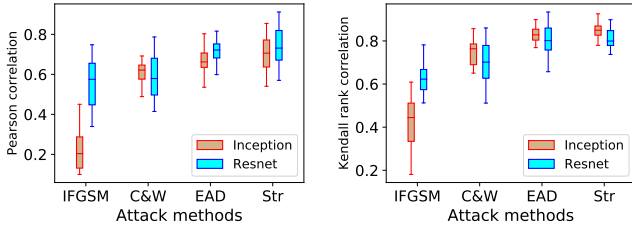


Figure 3: Correlation between sensitivity scores $\{s_i\}$ and ℓ_2 distortion values $\{\|\delta_{G_i}\|_2\}$. Left: Pearson correlation. Right: Kendall rank correlation.

and Str attacks exhibit a relatively stronger correlation than IFGSM since the latter perturbs every pixel due to the use of sign operation, while the former attacks are generated by ℓ_1 and ℓ_2 -norm penalized optimization methods that often yield non-uniform and sparser perturbations. For example, the sparsest Str-attack has the highest correlation since it perturbs discriminative image regions of high sensitivity (Xu et al. 2019b). In the next section, we will further connect pixel-level perturbations with discriminative image regions.

4 Interpreting Adversarial Perturbations via Class Activation Map (CAM)

CAM (Zhou et al. 2016) and other visual explanation techniques such as GradCAM (Selvaraju et al. 2017), Grad-CAM++ (Chattopadhyay et al. 2018) and RISE (Petsiuk, Das, and Saenko 2018) build a localizable deep representation, which exposes the implicit attention of CNNs on a labelled image (Zhou et al. 2016). In this section, we analyze the promotion-suppression effect (PSE) of adversarial perturbations via image-level interpretability. We restrict our analysis to CAM, but can readily be extended to other interpretability methods.

Let $F(\mathbf{x}, c)$ denote the CAM for image \mathbf{x} w.r.t. the class label c . The strength of a spatial element in $F(\mathbf{x}, c)$ characterizes the importance of the activation at this spatial location for classifying \mathbf{x} to the class c . Thus, one may wonder the relationship between adversarial examples and discriminative regions localized by CAM. Given natural and adversarial examples, CAMs of our interest include $F(\mathbf{x}_0, t_0)$, $F(\mathbf{x}', t_0)$, $F(\mathbf{x}_0, t)$ and $F(\mathbf{x}', t)$ with respect to both the correct and the target labels; see Figure 4 for an example and Figure A2 for more results. Figure 4 suggests that the effect of adversarial perturbations can be visually explained through the class-specific discriminative image regions localized by CAM. Compared $F(\mathbf{x}_0, t_0)$ with $F(\mathbf{x}', t_0)$, the most discriminative region w.r.t. (\mathbf{x}_0, t_0) is *suppressed* as δ is added to \mathbf{x}_0 . By contrast, the difference between $F(\mathbf{x}_0, t)$ and $F(\mathbf{x}', t)$ implies that the discriminative region of \mathbf{x}_0 under t is *enhanced* after injecting δ .

We next employ the so-called *interpretability score* (IS) (Xu et al. 2019b) to quantify how the adversarial perturbation δ is associated with the most discriminative image region found by the CAM $F(\mathbf{x}, c)$. More formally, let $B(\mathbf{x}, c)$ denote the Boolean map that highlights the most discrimina-

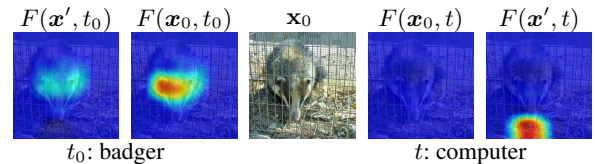


Figure 4: Visualizing CAMs of natural image and its adversarial example (generated by C&W attack) w.r.t. the true label ‘badger’ and the target label ‘computer’, respectively. The heat map color from blue to red represents the least and the most discriminative region localized by CAM, respectively. Here the values of CAMs are normalized w.r.t. the largest value cross CAMs.

tive region,

$$[B(\mathbf{x}, c)]_i = \begin{cases} 1 & [F(\mathbf{x}, c)]_i \geq \nu \\ 0 & \text{otherwise,} \end{cases} \quad (5)$$

where $\nu > 0$ is a given threshold, and $[F(\mathbf{x}, c)]_i$ is the i th element of $F(\mathbf{x}, c)$. The IS of adversarial perturbations w.r.t. (\mathbf{x}, c) is defined by

$$\text{IS}(\delta) = \|B(\mathbf{x}, c) \circ \delta\|_2 / \|\delta\|_2. \quad (6)$$

where \circ is the element-wise product. Figure A1 shows the sensitivity of IS against the hyperparameter ν . Not surprisingly, the threshold ν cannot be too large or too small to highlight the proper discriminative image regions. We set it as 70%-quantile of weights in a CAM.

In (6), $\text{IS}(\delta) \rightarrow 1$ if the discriminative region perfectly predicts the locations of adversarial perturbations. By contrast, if $\text{IS}(\delta) \rightarrow 0$, then adversarial perturbations cannot be interpreted by CAM. In Figure 5, we examine IS for 4 attack types via CAM, GradCAM++ and RISE w.r.t. (\mathbf{x}_0, t_0) and (\mathbf{x}', t) . We see that IS is not quite sensitive to the choice of interpretability methods, since it is built on Boolean localizable maps, which enjoy a large overlapping among different visual explanation tools. We also see that Str and IFGSM yield the best and the worst IS, respectively. These results are consistent with Figure 3: Str-attack tends to perturb local semantic image regions, while IFGSM perturbs every pixel due to the use of sign-based perturbation direction.

We recall that PSR in (4) categorizes $\{\delta_{G_i}\}$ into three types: suppression-dominated perturbations, promotion-dominated perturbations, and balanced perturbations. In

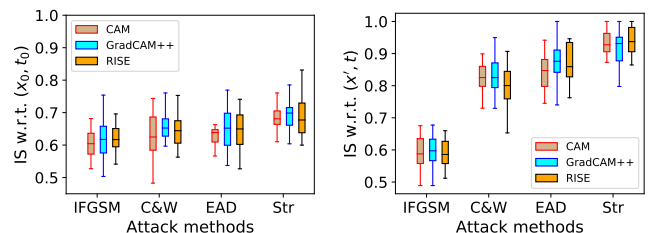


Figure 5: IS under 4 attack types & 3 visual explanation methods on Resnet. Left: IS defined on $F(\mathbf{x}_0, t_0)$. Right: IS defined on $F(\mathbf{x}', t)$. Each box plot represents IS values of 5000 natural/adversarial examples from ImageNet.

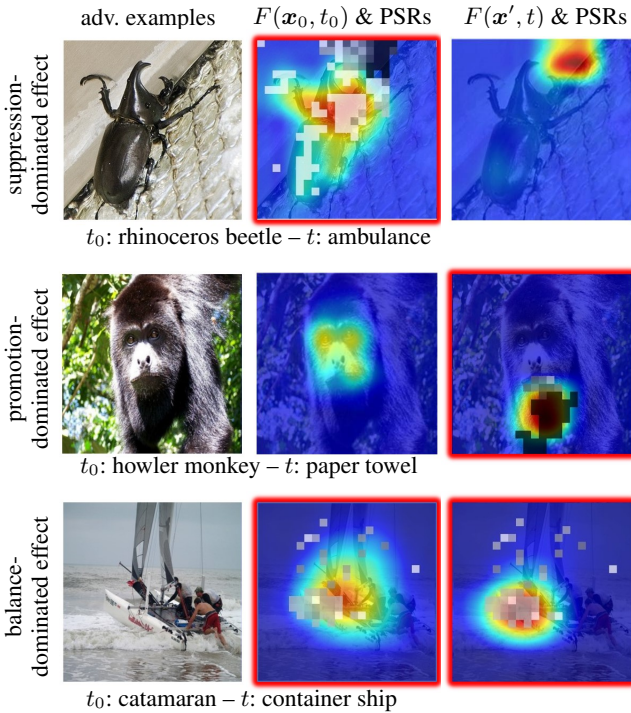


Figure 6: Interpreting adversarial perturbations via CAM and PSR. For PSR, only the top 70% most significant perturbed grids ranked by $\{s_i\}$ (3) are shown. The white and black colors represent the suppression-dominated regions ($r_i < -1$) and the promotion-dominated regions ($r_i > 1$), respectively. The gray color corresponds to balance-dominated perturbations ($r_i \in [-1, 1]$). And the red box represents the dominated adversarial effect.

Figure 6, we see that the locations and the promotion-suppression roles of adversarial perturbations are well matched to the discriminative regions of $F(\mathbf{x}_0, t_0)$ and $F(\mathbf{x}', t)$. In particular, if there exists a large overlapping between $F(\mathbf{x}_0, t_0)$ and $F(\mathbf{x}', t)$, then the balanced perturbations are desired since perturbing a single pixel can play a dual role in suppression and promotion. Toward deeper insights, we investigate how the adversary makes an impact on attacking a single image with multiple target labels (Figure 7) as well as attacking multiple images with the same source and target label (Figure A4). We see that the promotion-dominated perturbation is adaptive to the change of the target label in Figure 7. Moreover, the same source-target label pair enforces a similar effect of adversarial perturbations on attacking different images in Figure A4. Additional results can be found in Appendix 2.

Insights on how CAM constrains effectiveness of adversarial attacks. We have previously shown that CAM can be used to localize class-specific discriminative image regions. We now consider two types of CAM-based operations to refine an adversarial perturbation pattern: (a) removing less sensitive perturbations quantified by s_i in (3), and (b) enforcing perturbations in the most discriminative regions only w.r.t. the true label, namely, $B(\mathbf{x}_0, t_0)$ in (5). We represent the refinement operations (a) and (b) through the constraint



Figure 7: Interpreting adversarial examples of the original image ‘Japanese spaniel’ in Figure 1 w.r.t. different target labels ‘acoustic guitar’ and ‘desktop computer’ using CAM and PSR.

sets of pixels $\mathcal{S}_1 = \{\forall i | s_i > \beta\}$ for a positive threshold β and $\mathcal{S}_2 = \{\forall i | [B(\mathbf{x}_0, t_0)]_i > 0\}$, where β is set to filter perturbations of less than $1 - \nu = 30\%$ cumulative sensitivity scores. The refined adversarial examples are then generated by performing the existing attack methods with an additional projection on the sparse constraints given by \mathcal{S}_1 and \mathcal{S}_2 . We refer readers to Appendix 3 for more details.

We find that it is possible to obtain a more effective attack by perturbing much less pixels of high sensitivity scores under \mathcal{S}_1 , but without increasing ℓ_p perturbation strength (Table A1). For attacks with refinement under \mathcal{S}_2 , Figure 8 shows that perturbing pixels under only a suppression-dominated adversarial pattern \mathcal{S}_2 w.r.t. the true label is not effective: If we restrict perturbations under \mathcal{S}_2 , then the refined attack leads to a much larger ℓ_2 distortion. That is because the perturbation δ originally plays a role in promoting the confidence of the target label, which corresponds to a class-specific discriminative region different from \mathcal{S}_2 .

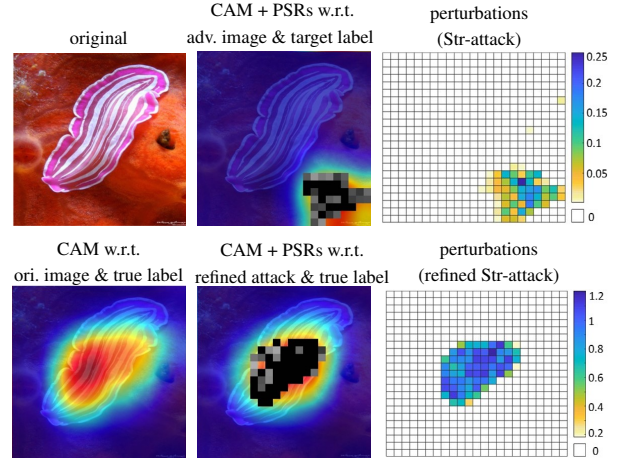


Figure 8: The ‘flatworm’-to-‘knot’ adversarial example (generated by str-Attack) with and without refinement under \mathcal{S}_2 . The first row presents the original image, PSRs overlaid on CAM of the adversarial example w.r.t. the target label ‘knot’, and the ℓ_2 -norm distortion of adversarial perturbations. The second row presents \mathcal{S}_2 given by CAM of the original image w.r.t. the true label ‘flatworm’, and the refined attack under \mathcal{S}_2 . Note that this refinement leads to much larger ℓ_2 distortion (max. value 1.2) against the unrefined attack (max. value 0.25); see the third column.

5 Seeing Effects of Adversarial Perturbations from Network Dissection

In this section, we examine the promotion-suppression effect of adversarial perturbations on the internal response of CNNs by leveraging network dissection (Bau et al. 2017). We show that there exists a connection between the sensitivity of units (a unit refers to a channel-wise feature map) and their concept-level interpretability.

We begin by reviewing the main idea of network dissection; see more details in (Bau et al. 2017). Interpretability measured by network dissection refers to the alignment between individual hidden units and a set of semantic concepts provided by the broadly and densely labeled dataset *Broden*. Different from other datasets, examples in Broden contain pixel-level concept annotation, ranging from low-level concepts such as *color* and *texture* to higher-level concepts such as *material*, *part*, *object* and *scene*. Network dissection builds a correspondence between a hidden unit’s activation and its interpretability on semantic concepts. More formally, the interpretability of unit (IoU) k w.r.t. the concept c is defined by (Bau et al. 2017)

$$\text{IoU}(k, c) = \frac{\sum_{\mathbf{x} \in \mathcal{D}} |\mathbf{M}_k(\mathbf{x}) \cap \mathbf{L}_c(\mathbf{x})|}{\sum_{\mathbf{x} \in \mathcal{D}} |\mathbf{M}_k(\mathbf{x}) \cup \mathbf{L}_c(\mathbf{x})|}, \quad (7)$$

where \mathcal{D} denotes Broden, and $|\cdot|$ is the cardinality of a set. In (7), $\mathbf{M}_k(\mathbf{x})$ is a binary segmentation of the activation map of unit k , which gives the representative region of \mathbf{x} at k . Here the activation is scaled up to the input resolution using bilinear interpolation, denoted by $\mathbf{S}_k(\mathbf{x})$, and then truncated using the top 5% quantile (dataset-level) threshold T_k . That is, $\mathbf{M}_k(\mathbf{x}) = \mathbf{S}_k(\mathbf{x}) \geq T_k$, namely, the (i, j) th element of $\mathbf{M}_k(\mathbf{x})$ is 1 if the (i, j) th element of $\mathbf{S}_k(\mathbf{x})$ is greater than or equal to T_k , and 0 otherwise. In (7), $\mathbf{L}_c(\mathbf{x})$ is the input-resolution annotation mask, provided by Broden, for the concept c w.r.t. \mathbf{x} . Since one unit might detect multiple concepts, the interpretability of a unit is summarized as $\text{IoU}(k) = (1/|\mathcal{C}|) \sum_c \text{IoU}(k, c)$, where $|\mathcal{C}|$ denotes the total number of concept labels.

We next investigate the effect of adversarial perturbations on the internal response of CNNs by leveraging network dissection. We produce adversarial examples \mathcal{D}' from Broden using the PGD untargeted attack method (Madry et al. 2017). Given adversarial examples $\{\mathbf{x}' \in \mathcal{D}'\}$, we characterize the sensitivity of unit k (to adversarial perturbations) via the change of activation segmentation

$$v(k) := \mathbb{E}_{(\mathbf{x}, \mathbf{x}')} [\|\mathbf{M}_k(\mathbf{x}) - \mathbf{M}_k(\mathbf{x}')\|_2], \quad (8)$$

where $(\mathbf{x}, \mathbf{x}')$ is a pair of natural and adversarial examples, and the expectation is taken over a certain distribution of our interest, e.g., the entire dataset or data of fixed source-target labels. In (8), we adopt the activation segmentation \mathbf{M}_k rather than the activation map \mathbf{S}_k since the former highlights the representative region of an activation map without inducing the layer-wise magnitude bias.

Given the per-unit sensitivity measure $v(k)$ and interpretability measure $\text{IoU}(k)$, we may ask *whether or not the sensitive units (to adversarial perturbations) exhibit strong interpretability*. To answer this question, we conduct the statistical significance test by contrasting the IoU of the top N ranked sensitive units with the IoU distribution of randomly

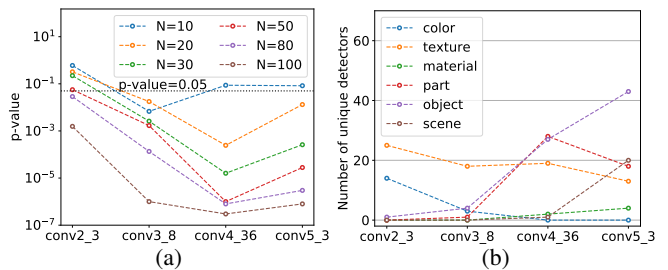


Figure 9: Sensitivity and interpretability. (a) p -value of interpretability of top N sensitive units to adversarial attacks in Resnet_152, where the presented layers include conv2_3 (256 units), conv3_8 (512 units), conv4_36 (1024 units) and conv5_3 (2048 units). (b) Number of concept detectors among top $N = 100$ sensitive units per layer for each concept category.

selected N units. Formally, the p -value is the probability of observing $\sum_k \text{IoU}(k)$ when k is from top N sensitive units ranked by $v(k)$ in the background IoU distribution when N units are randomly picked. The smaller the p -value is, the more significant the connection between sensitivity and interpretability is.

We present the significance test of the interpretability of top $N \in \{10, 20, 30, 50, 80, 100\}$ sensitive units against the layer index of Resnet_152 (Figure 9-a). We also show the number of concept detectors¹ among top $N = 100$ sensitive units versus layers for every concept category (Figure 9-b). Here we denote by conv_i_j the last convolutional layer of j th building block at the i th layer in Resnet_152 (He et al. 2016). It is seen from Figure 9-a that there exists a strong connection between the sensitivity of units and their interpretability since $p < 0.05$ in most of cases. By fixing the layer number, such a connection becomes more significant as N increases: Most of the top 100 sensitive units are interpretable, although the top 10 sensitive units might not be the same top 10 interpretable units. By fixing N , we observe that deep layers (conv4_36 and conv5_3) exhibit stronger connection between sensitivity and interpretability compared to shallow layers (conv2_3 and conv3_8). That is because the change of activation induced by adversarial attacks at shallow layers could be subtle and are less detectable in terms of interpretability. Indeed, Figure 9-b shows that more high-level concept detectors (e.g., object and part) emerge in conv4_36 and conv5_3 while low-level concepts (e.g., color and texture) dominate at lower layers.

To peer into the impact of adversarial perturbations on individual images, we examine how the representation of concept detectors change while facing adversarial examples by attacking images from the same true class t_0 to the same target class t . Here the representation of a concept detector is visualized by the segmented input image determined by $\mathbf{M}_k(\mathbf{x})$. In Figure 10, we show two examples of attacks: ‘table lamp’-to-‘studio couch, day bed’ and ‘airliner’-to-‘seashore, seacoast’. We first note that most of low-level concepts (e.g., color and texture) are detected at shallow layers, consistent with Figure 9-b. In the attack ‘table lamp’-to-‘studio couch, day bed’, the color ‘orange’ detected at

¹A concept detector refers to a unit with the top ranked concept satisfying $\max_c \text{IoU}(k, c) > 0.04$ (Bau et al. 2017).

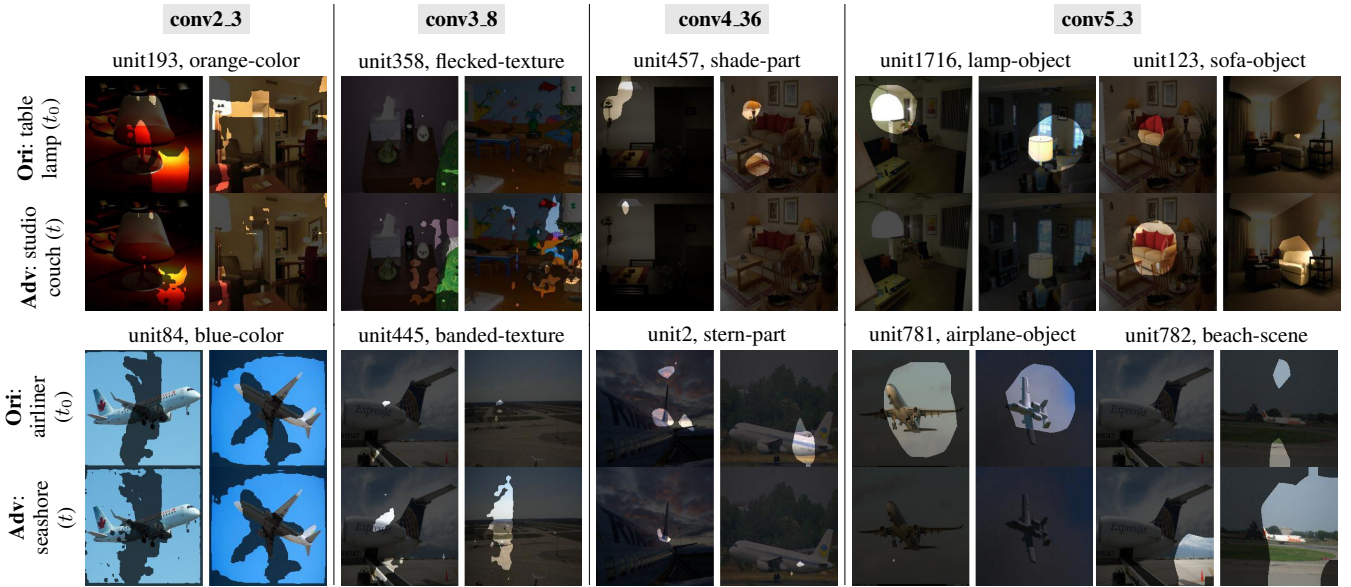


Figure 10: Visualizing impact of original (Ori) & adversarial (Adv) examples on the response of concept detectors identified by network dissection at 4 representative layers in Resnet. (top) attack ‘table lamp’-to-‘studio couch, day bed’, (bottom) attack ‘airliner’-to-‘seashore, seacoast’. In both top and bottom sub-figures, the first row presents unit indices together with detected top ranked concept labels and categories (in the format ‘concept label’-‘concept category’). The last two rows present the response of concept detectors visualized by the segmented input image, where the segmentation is given by $M_k(x)$ corresponding to the top ranked concept at each unit.

conv2_3 is less expressed for the adversarial image against the natural image. This aligns with human perception since ‘orange’ is related to ‘light’ and thus ‘table lamp’. By contrast, in the attack ‘airliner’-to-‘seashore, seacoast’, the color ‘blue’ is well detected at both natural and adversarial images, since ‘blue’ is associated with both ‘sky’ for ‘airliner’ and ‘sea’ for ‘seashore’. We also note that high-level concepts (e.g., part and object) dominate at deeper layers. At conv5_3, the expression of object concepts (e.g., lamp and airplane) relevant to the *true* label is *suppressed*. Meanwhile, the expression of object concepts (e.g., sofa and beach) relevant to the *target* label is *promoted*. This precisely reflects the activation promotion-suppression effect induced by adversarial perturbations. In Figure A8, we connect images in Figure 10 to PSR and CAM based visual explanation.

6 Insights of Interpretability for Improving Adversarial Robustness

First, PSE explains the effectiveness of detecting adversarial examples with feature attribution (Yang et al. 2019). It was shown in (Yang et al. 2019) that the input attribution scores of an adversarial example obtained by the leave-one-out method (Zeiler and Fergus 2014) yields a significantly larger variance than the case of natural image. The presence of a significant change on the probability of the top-1 class, when a pixel is removed from an adversarial example, is explainable. By PSE, the possible reason is that the seemingly random perturbation could play a critical role in promoting the confidence of the *target* label, e.g., Figure 7.

Second, hiding adversarial examples from CAM may be not easy. It was shown in (Zhang et al. 2018) that adversarial examples can be crafted to fool CNNs, and at the same time

keep their CAMs (w.r.t. the top-1 prediction class) intact. However, our results in Sec. 4 suggest that the discrepancy between CAMs of natural and adversarial examples exists w.r.t. *both* the true and the target label. Thus, we need to re-think whether or not it is easy to hide adversarial examples from network interpretation defined under the two-class or even all-class CAM distortion.

Third, network dissection implies the method of neuron masking to improve robustness. Since the sensitive units to adversarial perturbations exhibit strong interpretability, one could mitigate the effect of adversaries by masking these sensitive neurons with interpretation toward the target label. Our preliminary results in Table A2 of Appendix 4 show that the suggested neuron masking improves robustness at the cost of slight degradation on clean test accuracy.

7 Conclusions

In this work, we made a significant effort to understand the mechanism of adversarial attacks and provided its explanation at pixel, image and network levels. We showed that adversarial attacks play a significant role in activation promotion and suppression. The promotion-suppression effect is strongly associated with class-specific discriminative image regions. We also demonstrated that the interpretable adversarial pattern constrains the effectiveness of adversarial attacks. We further provided the first analysis of adversarial examples through network dissection, which builds the connection between the units’ sensitivity to imperceptible perturbations and their interpretability on semantic concepts. In the future, we would like to develop interpretability-driven defensive methods and consider the scenario of attack against interpretability, not just prediction.

References

- Athalye, A.; Carlini, N.; and Wagner, D. 2018. Obfuscated gradients give a false sense of security: Circumventing defenses to adversarial examples. *arXiv preprint arXiv:1802.00420*.
- Bau, D.; Zhou, B.; Khosla, A.; Oliva, A.; and Torralba, A. 2017. Network dissection: Quantifying interpretability of deep visual representations. *arXiv preprint arXiv:1704.05796*.
- Bau, D.; Zhu, J.-Y.; Strobelt, H.; Zhou, B.; Tenenbaum, J. B.; Freeman, W. T.; and Torralba, A. 2019. Visualizing and understanding generative adversarial networks. In *International Conference on Learning Representations*.
- Boyd, S.; Parikh, N.; Chu, E.; Peleato, B.; Eckstein, J.; et al. 2011. Distributed optimization and statistical learning via the alternating direction method of multipliers. *Foundations and Trends® in Machine Learning* 3(1):1–122.
- Brown, T. B.; Mané, D.; Roy, A.; Abadi, M.; and Gilmer, J. 2017. Adversarial patch. *arXiv preprint arXiv:1712.09665*.
- Carlini, N., and Wagner, D. 2017a. Adversarial examples are not easily detected: Bypassing ten detection methods. In *Proceedings of the 10th ACM Workshop on Artificial Intelligence and Security*, 3–14. ACM.
- Carlini, N., and Wagner, D. 2017b. Towards evaluating the robustness of neural networks. In *Security and Privacy (SP), 2017 IEEE Symposium on*, 39–57. IEEE.
- Carlini, N.; Mishra, P.; Vaidya, T.; Zhang, Y.; Sherr, M.; Shields, C.; Wagner, D.; and Zhou, W. 2016. Hidden voice commands. In *USENIX Security Symposium*, 513–530.
- Carter, S.; Armstrong, Z.; Schubert, L.; Johnson, I.; and Olah, C. 2019. Activation atlas. *Distill*. <https://distill.pub/2019/activation-atlas>.
- Chattopadhyay, A.; Sarkar, A.; Howlader, P.; and Balasubramanian, V. N. 2018. Grad-cam++: Generalized gradient-based visual explanations for deep convolutional networks. In *2018 IEEE Winter Conference on Applications of Computer Vision (WACV)*, 839–847. IEEE.
- Chen, P.-Y.; Sharma, Y.; Zhang, H.; Yi, J.; and Hsieh, C.-J. 2017. Ead: elastic-net attacks to deep neural networks via adversarial examples. *arXiv preprint arXiv:1709.04114*.
- Dong, Y.; Su, H.; Zhu, J.; and Bao, F. 2017. Towards interpretable deep neural networks by leveraging adversarial examples. *arXiv preprint arXiv:1708.05493*.
- Finlay, C.; Oberman, A.; and Abbasi, B. 2018. Improved robustness to adversarial examples using lipschitz regularization of the loss. *arXiv preprint arXiv:1810.00953*.
- Goodfellow, I.; Shlens, J.; and Szegedy, C. 2015. Explaining and harnessing adversarial examples. *2015 ICLR arXiv preprint arXiv:1412.6572*.
- He, K.; Zhang, X.; Ren, S.; and Sun, J. 2016. Deep residual learning for image recognition. In *Proceedings of the IEEE conference on computer vision and pattern recognition*, 770–778.
- Karmon, D.; Zoran, D.; and Goldberg, Y. 2018. Lavan: Localized and visible adversarial noise. *arXiv preprint arXiv:1801.02608*.
- Kurakin, A.; Goodfellow, I.; and Bengio, S. 2016. Adversarial examples in the physical world. *arXiv preprint arXiv:1607.02533*.
- Kurakin, A.; Goodfellow, I. J.; and Bengio, S. 2017. Adversarial machine learning at scale. *2017 ICLR arXiv preprint arXiv:1611.01236*.
- Luo, T.; Cai, T.; Zhang, M.; Chen, S.; and Wang, L. 2018. Random mask: Towards robust convolutional neural networks.
- Madry, A.; Makelov, A.; Schmidt, L.; Tsipras, D.; and Vladu, A. 2017. Towards deep learning models resistant to adversarial attacks. *arXiv preprint arXiv:1706.06083*.
- Papernot, N.; McDaniel, P.; Jha, S.; Fredrikson, M.; Celik, Z. B.; and Swami, A. 2016a. The limitations of deep learning in adversarial settings. In *Security and Privacy (EuroS&P), 2016 IEEE European Symposium on*, 372–387. IEEE.
- Papernot, N.; McDaniel, P.; Wu, X.; Jha, S.; and Swami, A. 2016b. Distillation as a defense to adversarial perturbations against deep neural networks. In *Security and Privacy (SP), 2016 IEEE Symposium on*, 582–597. IEEE.
- Petsiuk, V.; Das, A.; and Saenko, K. 2018. Rise: Randomized input sampling for explanation of black-box models. *arXiv preprint arXiv:1806.07421*.
- Selvaraju, R. R.; Cogswell, M.; Das, A.; Vedantam, R.; Parikh, D.; and Batra, D. 2017. Grad-cam: Visual explanations from deep networks via gradient-based localization. In *Proceedings of the IEEE International Conference on Computer Vision*, 618–626.
- Sinha, A.; Namkoong, H.; and Duchi, J. 2018. Certifying some distributional robustness with principled adversarial training.
- Szegedy, C.; Vanhoucke, V.; Ioffe, S.; Shlens, J.; and Wojna, Z. 2016. Rethinking the inception architecture for computer vision. *2016 IEEE Conference on Computer Vision and Pattern Recognition (CVPR)* 2818–2826.
- Xiao, C.; Zhu, J.-Y.; Li, B.; He, W.; Liu, M.; and Song, D. 2018. Spatially transformed adversarial examples. In *International Conference on Learning Representations*.
- Xu, K.; Chen, H.; Liu, S.; Chen, P.-Y.; Weng, T.-W.; Hong, M.; and Lin, X. 2019a. Topology attack and defense for graph neural networks: An optimization perspective. In *International Joint Conference on Artificial Intelligence (IJCAI)*.
- Xu, K.; Liu, S.; Zhao, P.; Chen, P.-Y.; Zhang, H.; Fan, Q.; Erdogmus, D.; Wang, Y.; and Lin, X. 2019b. Structured adversarial attack: Towards general implementation and better interpretability. In *International Conference on Learning Representations*.
- Yang, P.; Chen, J.; Hsieh, C.-J.; Wang, J.-L.; and Jordan, M. I. 2019. MI-loo: Detecting adversarial examples with feature attribution. *arXiv preprint arXiv:1906.03499*.
- Ye, S.; Xu, K.; Liu, S.; Cheng, H.; Lambrechts, J.-H.; Zhang, H.; Zhou, A.; Ma, K.; Wang, Y.; and Lin, X. 2019. Adversarial robustness vs model compression, or both? *International Conference on Computer Vision (ICCV-2019)*.
- Yu, F.; Dong, Q.; and Chen, X. 2018. Asp: A fast adversarial attack example generation framework based on adversarial saliency prediction. *arXiv preprint arXiv:1802.05763*.
- Yuan, M., and Lin, Y. 2006. Model selection and estimation in regression with grouped variables. *Journal of the Royal Statistical Society: Series B (Statistical Methodology)* 68(1):49–67.
- Zeiler, M. D., and Fergus, R. 2014. Visualizing and understanding convolutional networks. In *European conference on computer vision*, 818–833. Springer.
- Zhang, X.; Wang, N.; Ji, S.; Shen, H.; and Wang, T. 2018. Interpretable deep learning under fire. *arXiv preprint arXiv:1812.00891*.
- Zhou, B.; Khosla, A.; Lapedriza, A.; Oliva, A.; and Torralba, A. 2016. Learning deep features for discriminative localization. In *Proceedings of the IEEE Conference on Computer Vision and Pattern Recognition*, 2921–2929.

Appendices of *Interpreting Adversarial Examples by Activation Promotion and Suppression*

1 Attack Generation

IFGSM attack (Goodfellow, Shlens, and Szegedy 2015; Kurakin, Goodfellow, and Bengio 2017) produces adversarial examples by performing iterative fast gradient sign method (IFGSM), followed by an ϵ -ball clipping. IFGSM attacks are designed to be fast, rather than optimal in terms of minimum perturbation.

C&W (Carlini and Wagner 2017a), **EAD** (Chen et al. 2017), and **Str-attacks** (Xu et al. 2019b) can be unified in the following optimization framework,

$$\begin{aligned} & \underset{\delta}{\text{minimize}} && f(\mathbf{x}_0 + \delta, t) + \lambda g(\delta) \\ & \text{subject to} && (\mathbf{x}_0 + \delta) \in [0, 1]^n, h(\delta) \leq 0, \end{aligned} \quad (9)$$

where $f(\mathbf{x}_0 + \delta, t)$ denotes a loss function for targeted misclassification, $g(\delta)$ is a regularization function that penalizes the norm of adversarial perturbations, $\lambda > 0$ is a regularization parameter, and $h(\delta)$ places optionally hard constraints on δ . All C&W, EAD and Str-attacks enjoy a similar loss function

$$f(\mathbf{x}_0 + \delta, t) = c \cdot \max\left\{ \max_{j \neq t} Z(\mathbf{x}_0 + \delta)_j - Z(\mathbf{x}_0 + \delta)_t, -\kappa \right\}, \quad (10)$$

where $Z(\mathbf{x})_j$ is the j -th element of logits $Z(\mathbf{x})$, namely, the output before the last softmax layer in CNNs, and κ is a confidence parameter. Clearly, as κ increases, the minimization of f would reach the target label with high confidence. In this paper, we set $\kappa = 1$ by default. It is worth mentioning that problem (9) can be efficiently solved via alternating direction method of multipliers (ADMM) (Boyd et al. 2011; Xu et al. 2019b), regardless of whether or not $g(\delta)$ is differentiable.

C&W attack (Carlini and Wagner 2017a) adopts the ℓ_p norm to penalize the strength of adversarial perturbations δ , namely, $g(\delta) = \|\delta\|_p$ and $h(\delta) = 0$ in (9), where $p \in \{0, 2, \infty\}$. In practice, the squared ℓ_2 norm is commonly used.

EAD attack (Chen et al. 2017) specifies the regularization term $\lambda g(\delta)$ as an elastic-net regularizer $\lambda_1 \|\delta\|_2^2 + \lambda_2 \|\delta\|_1$ in (9), and $h(\delta) = 0$. It has empirically shown that the use of elastic-net regularizer improves the transferability of adversarial examples.

Str-attack (Xu et al. 2019b) takes into account the group-level sparsity of adversarial perturbations by choosing $g(\delta)$ as the group Lasso penalty (Yuan and Lin 2006). In the mean time, it constrains the pixel-level perturbation by setting $h(\delta) = \|\delta\|_\infty - \epsilon$ for a tolerance $\epsilon > 0$.

2 CAM-based Interpretation

Sensitivity of hyper-parameter ν to IS. Figure A1 presents IS against ν for IFGSM, C&W, EAD and Str attacks.

Additional results on CAM-based interpretation. In Figure A2, we demonstrate more examples of class-specific discriminative regions visualized by CAM, namely, $F(\mathbf{x}', t_0)$, $F(\mathbf{x}_0, t_0)$, \mathbf{x}_0 , $F(\mathbf{x}_0, t)$, $F(\mathbf{x}', t)$. In Figure A3, we fix the

original image together with its true and target labels to visualize the difference of attack methods through CAM. In Figure A4, we present the adversarial attack of multiple images with a fixed source-target label pair. As we can see, the balance-dominated perturbation pattern appears at the discriminative region of ‘eagle’. In Figure A5, we present the ‘hamster’-to-‘cup’ example, where objects of the original label and the target label exist simultaneously. We observe that the adversary shows suppression on the discriminative region of the original label and promotion on the discriminative region of the target label. Compared to the C&W attack, Str-attack is more effective in both suppressing and promotion since it perturbs less pixels. In Figure A6, images involve more heterogeneous and complex backgrounds. As we can see, an effective adversarial attack (e.g., Str-attack) perturbs less but more meaningful pixels, which have a better correspondence with the discriminative image regions of the original and target classes. In Figure A7, we present a ‘hippocampus’-to-‘streetcar’ example with refined attacks under \mathcal{S}_1 . As we can see, it is possible to obtain a more effective attack by perturbing less but ‘right’ pixels (i.e., with better correspondence with discriminative image regions).

3 Effectiveness of Refined Adversarial Pattern

We consider the following unified optimization problem to refine adversarial attacks

$$\begin{aligned} & \underset{\delta}{\text{minimize}} && f(\mathbf{x}_0 + \delta, t) + \lambda g(\delta) \\ & \text{subject to} && (\mathbf{x}_0 + \delta) \in [0, 1]^n, h(\delta) \leq 0 \\ & && \delta_i = 0, \text{ if } i \notin \mathcal{S}_k, k = 1 \text{ or } 2, \end{aligned} \quad (11)$$

where we represent the refinement operations (a) and (b) through the constraint sets $\mathcal{S}_1 = \{\forall i \mid s_i > \beta\}$ for a positive threshold β ² and $\mathcal{S}_2 = \{\forall i \mid [B(\mathbf{x}_0, t_0)]_i > 0\}$. In \mathcal{S}_1 , s_i defined by (3) characterizes the strength of the adversarial pattern. In \mathcal{S}_2 , $B(\mathbf{x}_0, t_0)$ defined by (5) localizes pixels corresponding to the most discriminative region associated with the true label. Problem (11) can similarly be solved as (9), with an additional projection on the sparse constraints given by \mathcal{S}_1 and \mathcal{S}_2 .

We present the effectiveness of attacks with refinement under \mathcal{S}_1 in Table A1. Here the effectiveness of an attack is characterized by its attack success rate (ASR) as well as ℓ_p -norm distortions. We find that many pixel-level adversarial perturbations are redundant, in terms of the reduction in the ℓ_0 norm³ of δ , which can be removed without losing effectiveness in the attack success rate and ℓ_p -norm distortions for $p > 0$.

4 Interpretation via Network Dissection

In Figure A8, we connect images in Figure 10 to PSR and CAM based visual explanation. For example, the suppressed image region identified by PSR (white color) corresponds

²We sort $\{s_i\}$ to $\{\tilde{s}_i\}$ in an ascending order, and set $\beta = \tilde{s}_k$ for the smallest k with $\sum_{i=1}^k \tilde{s}_i / \sum_{i=1}^m \tilde{s}_i \geq 30\%$. We filter less significant perturbations under their cumulative power.

³ $\|\mathbf{x}\|_0$: # of nonzero elements in \mathbf{x} .

to the interpretable activation of object concept airplane in Figure 10. And the promoted image region identified by PSR (black color) corresponds to the interpretable activation of scene concept beach.

In Table A2, we report the clean test accuracy (CTA) and the adversarial test accuracy (ATA) under three masking settings on the last convolutional layer of `conv5`: a) our proposed masking over top 10 sensitive units with concept-level interpretability, b) random masking over 10 units, and c) no masking. ATA is obtained by perturbing 1000 randomly selected test images using k -step PGD attack (Madry et al. 2017), where $k \in \{10, 20, 50, 100\}$. Our preliminary results show that the proposed approach yields the highest ATA, balanced with slight degradation on CTA.

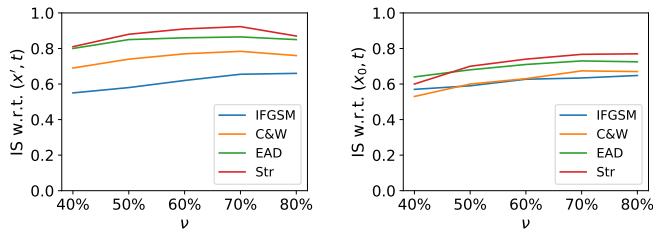


Figure A1: IS versus ν for 4 attack types.

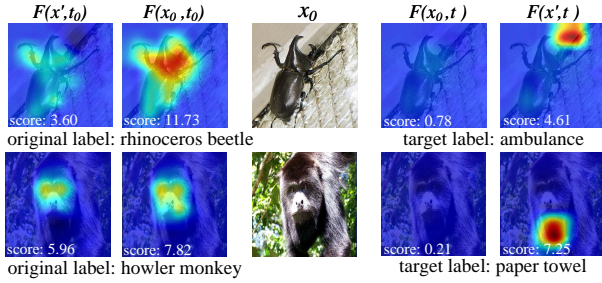


Figure A2: CAMs of two natural/adversarial examples (in rows), generated by C&W attack, where $F(\mathbf{x}', t_0)$, $F(\mathbf{x}_0, t_0)$, \mathbf{x}_0 , $F(\mathbf{x}_0, t)$, $F(\mathbf{x}', t)$ are shown from the left to the right at each row.

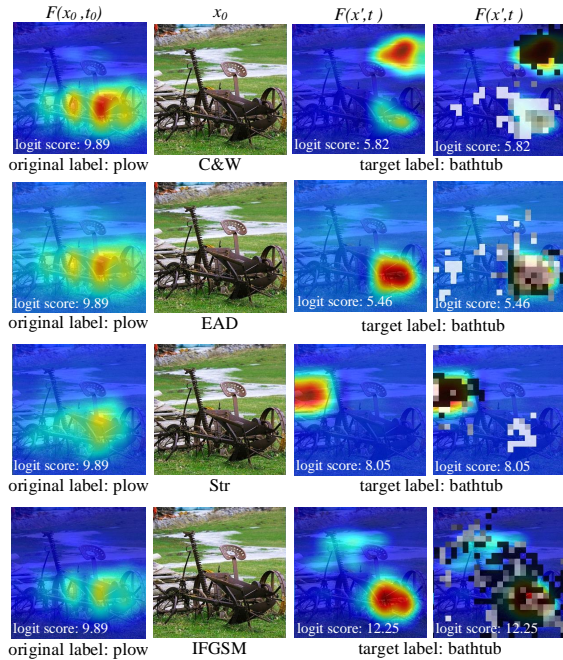


Figure A3: Four adversarial examples with CAM visualization generated by C&W, EAD, Str, and IFGSM attacks, respectively. Left to right: $F(\mathbf{x}_0, t_0)$, \mathbf{x}_0 , $F(\mathbf{x}', t)$, and overlaid PSR r_i on $F(\mathbf{x}', t)$ at locations of the top 70% most significant perturbed grids ranked by s_i . Here CAMs at each row are normalized with respect to their maximum value.

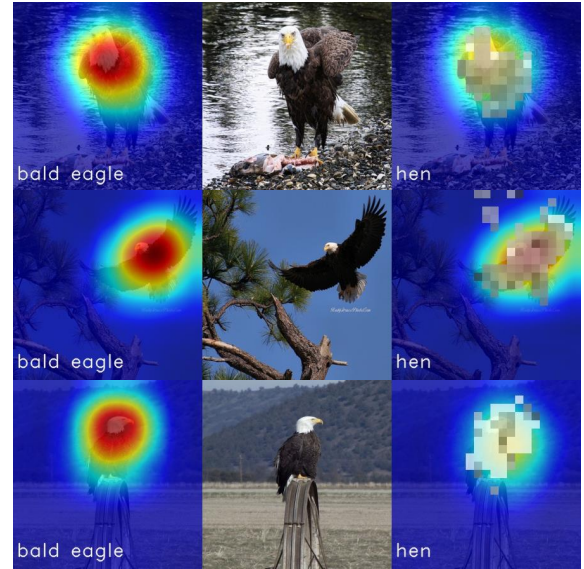


Figure A4: Multiple images with a fixed source-target label pair: CAM with respect to the source label 'bald eagle' (1 column), original image 'bald eagle' (2 column), CAM with respect to target label 'hen' together with C&W perturbation patterns (3 column), which is measured by promotion-suppression ratio (PSR), i.e. suppression- (white), promotion- (black), and balance-dominated adversaries (gray).

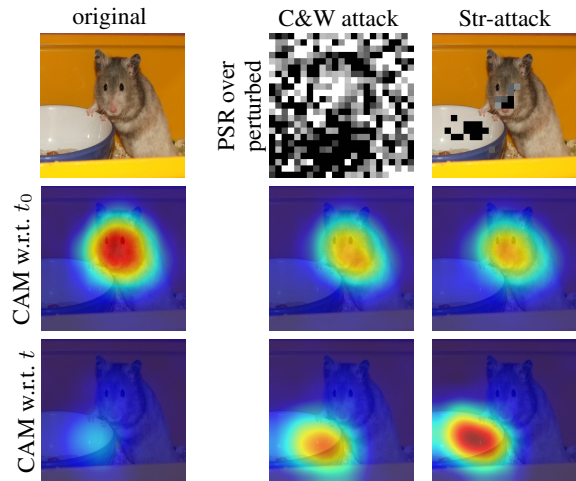


Figure A5: Visual explanation of the 'hamster'-to-'cup' example crafted by C&W and Str-attack, where the true label t_0 is 'hamster', and the target label t is 'cup'. The first row is the natural image and PSRs over perturbed grids. The second (third) row is CAM and PSRs with respect to the column-wise natural/adversarial example and the row-wise label.

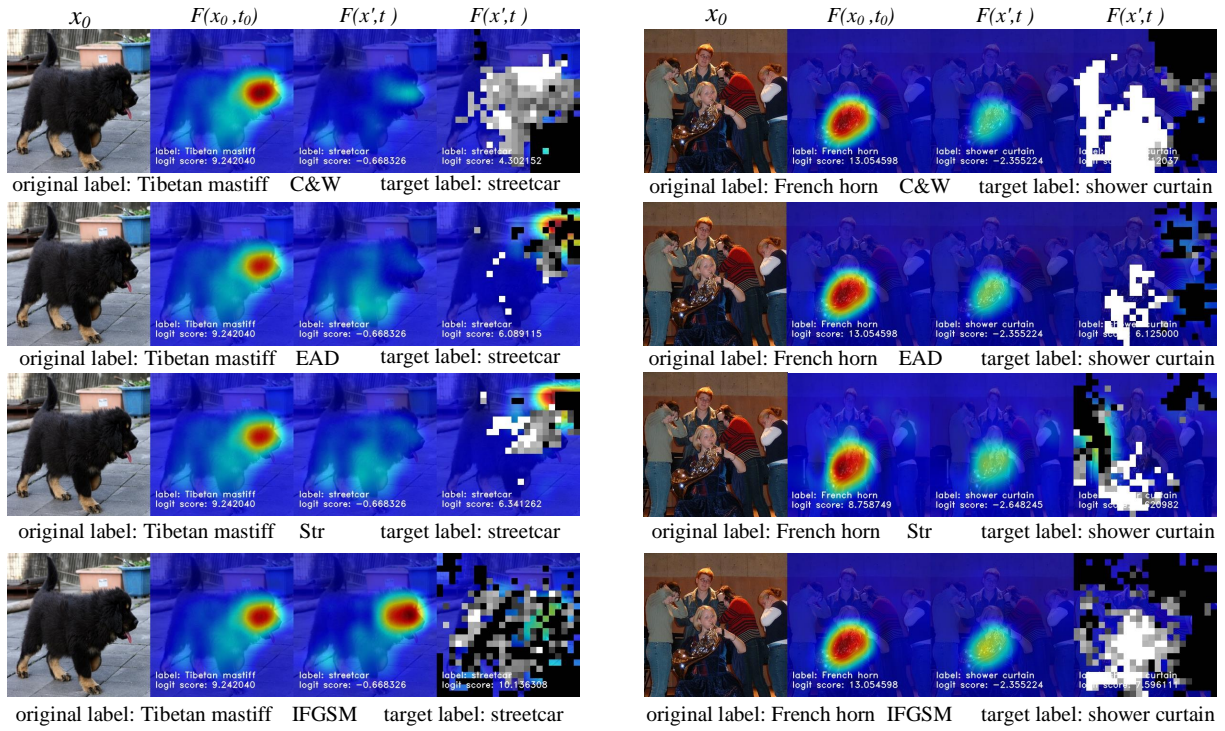


Figure A6: Attacking images with complex background under C&W, EAD, Str-, and IFGSM attacks.

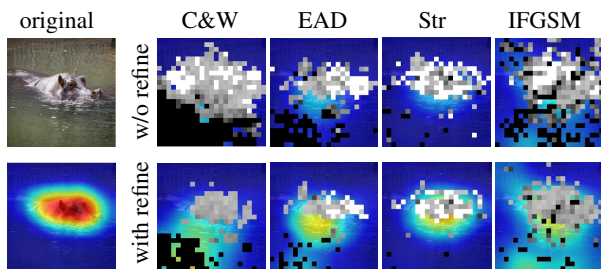


Figure A7: The 'hippopotamus'-to-'streetcar' adversarial example with and without refinement under \mathcal{S}_1 . Here the left-bottom subplot shows CAM of the original image w.r.t. the true label 'hippopotamus', and the right subplots present PSRs of unrefined and refined grid-level perturbations overlaid on CAMs of adversarial examples w.r.t. the target label 'streetcar'.

Table A1: Attack performance of adversarial perturbations with and without refinement under \mathcal{S}_1 over 5000 images.

attack	model	ℓ_0		ℓ_1		ℓ_2		ℓ_∞		ASR
		original (δ)	refine (δ_S)	original	refine	original	refine	original	refine	refine
IFGSM	Resnet	266031	61055	1122.56	176.08	2.625	1.87	0.017	0.035	96.7%
	Incep.	266026	59881	812.94	155.89	1.926	1.22	0.019	0.033	100%
C&W	Resnet	268117	21103	183.65	134.26	0.697	0.727	0.028	0.029	100%
	Incep.	268123	22495	144.94	96.75	0.650	0.673	0.028	0.034	100%
EAD	Resnet	66584	20147	42.57	63.28	1.520	1.233	0.234	0.096	100%
	Incep.	69677	18855	30.17	45.88	1.289	1.107	0.229	0.083	100%
Str	Resnet	30823	18744	119.76	110.54	1.250	1.132	0.105	0.087	100%
	Incep.	27873	15967	86.55	82.33	1.174	0.985	0.103	0.072	100%

Table A2: Evaluation of neuron masking on clean test accuracy (CTA) and adversarial test accuracy (ATA) against k -step PGD attacks.

	CTA	ATA (10-PGD)	ATA (20-PGD)	ATA (50-PGD)	ATA (100-PGD)
ours	75.9%	60.1%	51.5%	39.7%	33.6%
random masking	77.0%	40.5%	28.7%	18.3%	14.3%
no masking	78.2%	41.7%	31.0%	18.8%	15.7%

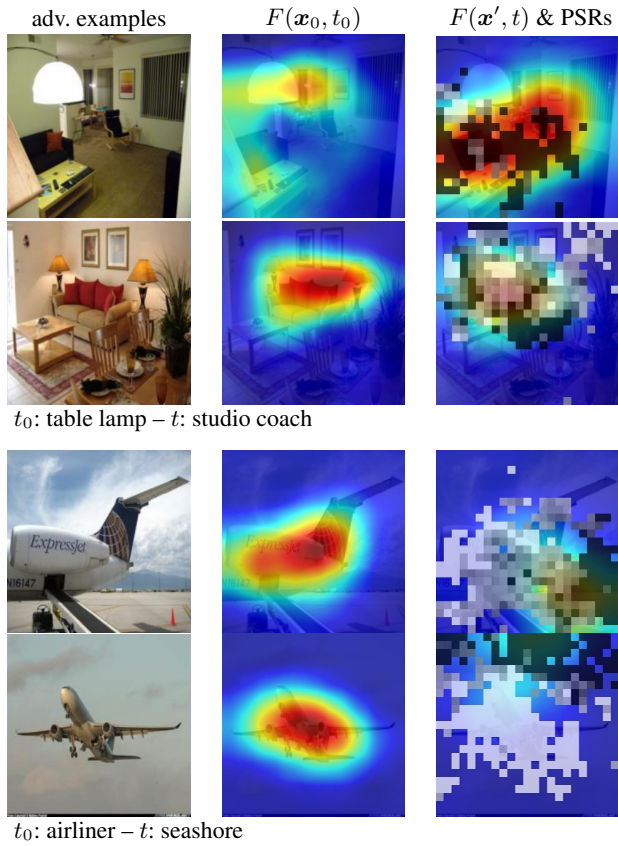


Figure A8: Interpreting adversarial perturbations via CAM and PSR. Image examples are from Figure 10. For PSR, only the top 70% most significant perturbed grids ranked by $\{s_i\}$ (3) are shown. The white and black colors represent the suppression-dominated regions ($r_i < -1$) and the promotion-dominated regions ($r_i > 1$), respectively. The gray color corresponds to balance-dominated perturbations ($r_i \in [-1, 1]$).